Journal of Biomechanical Engineering. Received December 06, 2022;
Accepted manuscript posted August 03, 2023. doi:10.1115/1.4063088

Shreyas Sarfare
Department of Mechanical Engineering,
Texas A&M University

MD Shujan Ali
Department of Mechanical Engineering,
Texas A&M University

Alan Palazzolo[1]
Department of Mechanical Engineering,
Texas A&M University

Mark Rodefeld
Indiana University School of Medicine

Tim Conover and Richard Figliola
Department of Mechanical & Bioengineering,
Clemson University

Guruprasad Giridharan
Department of Bioengineering,
University of Louisville

Rich Wampler
Consultant

Ed Bennett and Artem Ivashchenko
Mechanical Solutions, Inc.

CFD Turbulence Model and Experimental Study for a Fontan Cavopulmonary Assist Device

Head-flow HQ curves for a Fontan cavopulmonary assist device (CPAD) were measured using a blood surrogate in a mock circulatory loop and simulated with various computational fluid dynamics (CFD) models. The tests benchmarked the CFD tools for further enhancement of the CPAD design. Recommended Reynolds-Averaged Navier-Stokes (RANS) CFD approaches for the development of conventional ventricular assist devices (VAD). These were found to have shortcomings when applied to the Fontan CPAD, designed to neutralize off-condition obstruction risks that could contribute to a major adverse event. The no-obstruction condition is achieved with a von Karman pump, utilizing large clearances and small blade heights, which challenge conventional VAD RANS-based CFD hemodynamic simulations. High-fidelity Large Eddy Simulation (LES) is always recommended; however, this may be cost-inhibitive for optimization studies in commercial settings, thus the reliance on RANS models. This study compares head and power predictions of various RANS turbulence models, employing experimental measurements and LES results as a basis for comparison. The models include standard $k-\epsilon$, RNG $k-\epsilon$, Realizable $k-\epsilon$, SST $k-\omega$, SST with transitional turbulence, and Generalized $k-\omega$. For the pressure head predictions, it was observed that the standard $k-\epsilon$ model provided far better agreement with experiment. For the rotor torque, $k-\epsilon$ predictions were 30% lower than LES, while the SST and LES torque values were near identical. For the Fontan CPAD, the findings support using LES for the final design simulations, $k-\epsilon$ model for head and general flow simulation, and SST for power, shear stress, hemolysis, and thrombogenicity predictions.

Keywords: Fontan, Cavopulmonary Assist Device, Computational Fluid Dynamics, Blood pump, RANS Turbulence models, Large Eddy Simulation

1 Introduction

A small but significant number of infants are born with a single functional ventricle. This condition is surgically palliated by a series of staged operations that are timed to coincide with somatic growth and physiologic maturation. Ultimately, this results in a Fontan circulation in which the superior and inferior venae cavae are coupled to the pulmonary arteries in a cruciform junction [1]. This routes systemic venous blood to the pulmonary circulation, however, there is no subpulmonary power source, and the driving pressure depends on residual systemic venous pressure to drive blood flow through the lungs. It is an inherently inefficient circulatory system in which the systemic venous pressure is abnormally elevated, and preload to the systemic ventricle is reduced, resulting in reduced cardiac output. We have hypothesized that the reinstatement of a subpulmonary power source in a Fontan circulation (a cavopulmonary assist device; CPAD) will remedy this problem and restore a normal circulatory state [2].

The use of CFD has become widespread in the development and optimization of several engineering devices including medical implants, automobiles, pumps [3], compressors [4], and electronics cooling solutions [5]. CFD-based design optimization has been used extensively in the development of medical devices to evaluate hydraulic as well as hemodynamic design requirements [6]. An important consideration is the choice of modeling approach to assess the pump performance and is controversial. The most common turbulence models are Reynolds-Averaged Navier-Stokes (RANS) based models, such as $k-\epsilon$, $k-\omega$, Shear stress transport (SST), and others. The mean motion of the flow is considered in these models, instead of solving for the instantaneous flow. An alternative is either Direct Numerical Simulation (DNS), Large Eddy Simulation (LES), or a hybrid model that combines RANS and LES methodologies (e.g., Detached Eddy Simulation – DES). In DNS, all spatial and temporal scales of turbulence are resolved, without any turbulence model. In LES, only the large eddies are resolved, and the small eddies are modeled. However, these high-fidelity models are computationally expensive. Even with the development of sophisticated modeling techniques, the best turbulence model to characterize blood flow in a medical device remains debatable. Also, due to the uncertainty in the choice of turbulence model, validation with experimental data is often required. The goal of this study is to evaluate various RANS turbulence models in terms of their prediction accuracy by comparing them to experimental data and LES predictions, for the Fontan CPAD.

The $k-\epsilon$ model is one of the most commonly used turbulence models in CFD. In recent years, it has been widely used in CFD modeling of medical devices with good results. Chua et al. [7] used the $k-\epsilon$ model to model the Kyoto-NTN centrifugal pump. The predicted pressure head was about 8.3% lower than in experiments. The $k-\epsilon$ model had better agreement with experimental results as compared to a laminar model for a continuous flow VAD [8]. It correlated within 15% of experimental velocity measurements for the HeartQuest continuous flow LVAD [9], and within 10% of experimental measurements for an axial flow LVAD [10]. Anderson et al. [11] used the $k-\epsilon$ model to study a CFVAD and the predicted flow curves closely matched the corresponding experimental curves at low pump flow rates.

The SST turbulence model is another commonly used turbulence model, particularly for modeling rotating machines. Kido et al. [12] implemented the $k-\omega$ SST model to compute the flow in the

[1]Corresponding Author.
July 3, 2023

Tiny Pump. Wu et al. [13] used it for analyzing a centrifugal VAD. Bluestein [14] used the $k-\omega$ model since the $k-\epsilon$ model produced inferior predictions for some low-Re flows. SST modeling has been shown to provide good agreement with test measurements in conventional high-performance pumps and compressors that utilize tight tip clearances to boost efficiency [15–17].

The LES approach was used by Delorme et.al. [18] to model the total cavopulmonary connection (TCPC) cruciform of a Fontan CPAD. Two of the three velocity components showed excellent agreement between simulation and test for the no-pump case. Reasonable agreement was attained for measurements away from the pump impeller. The experimental results did not include measurement of the pump's head vs. flowrate curves. A wall shear stress study was also conducted with their LES model. The results confirmed shear stress levels well below those associated with incipient hemolysis. Delorme et al. [19] extended their LES modeling of the Fontan CPAD using a multi-block parallel processing approach to reduce computation time. Complex patient-specific geometries with the implanted CPAD were segmented with multi-block structures to provide efficient LES modeling with a simple Cartesian mesh. Their work did not undertake a comparative study comparing the results of the LES and RANS models.

Laminar (no turbulence) flow models have also been employed for modeling VADs. Burgreen et al. [20] used a laminar model for analyzing the Heartmate III LVAD, where CFD predicted the pressure head within 10% of the experimental values. Zhang et al. [21] used it to analyze a magnetically levitated VAD. The computationally predicted pressure head was in good agreement with the experimentally measured value.

Several studies have compared turbulence models for the analysis of flows through centrifugal heart pumps. Song et al. [22] studied various turbulence models for the CF4 LVAD. The $k-\omega$ model showed a better agreement with PIV measurements, especially around the near-wall regions. The $k-\epsilon$, $k-\omega$, and SST $k-\omega$ models were compared by Throckmorton et al. [23] for PVAD3. The $k-\epsilon$ results were in the best agreement with experimental measurements of bulk hydraulic properties. Al-Azawy et al. [24] compared the $k-\epsilon$, $k-\omega$, SST, and Reynolds stress model (RSM) for a pulsatile flow VAD in which the RSM provided the most accurate description over much of the flow domain. Zhang et al. [6] investigated the $k-\epsilon$ (standard and RNG), Spalart-Almaras, $k-\omega$, SST, and RSM turbulence models for a clinically used VAD. RNG $k-\epsilon$ and the RSM models were found to be the most accurate. For a pulsatile pump LVAD [25], among the RSM, SST $k-\omega$, transitional SST, and laminar models, RSM gave the best agreement with experimental results. Lui et al. [26] studied blood flow in a stenotic vessel using DNS and RANS turbulence models ($k-\epsilon$, $k-\omega$, and a transitional three-equation eddy-viscosity model) and found that the transitional RANS model provided results closer to DNS than the other two models. Wang et al. [27] studied an axial flow blood pump operating at 8000 RPM using the standard $k-\epsilon$, RNG $k-\epsilon$, $k-\omega$, and SST $k-\omega$ turbulence models, and found that the SST $k-\omega$ model had the smallest average error for the velocity field. Semenzin et al. [28] recommend using a hybrid RANS-LES turbulence model, particularly the Stress-Blended Eddy Simulation (SBES) model for simulating flow in rotary blood pumps based on their findings on modeling the FDA centrifugal pump. Among the RANS models analyzed in the study, the $k-\omega$ model predicted the pressure within 5% of the experimental results but had shortcomings in modeling the velocity field.

Computational models are not only sensitive to solving schemes, and spatial and temporal resolution, but also to the choice of turbulence model. From the above studies, it is evident that there is no universal turbulence model to accurately predict the flow fields and other quantities of interest in biomedical devices, even within devices of similar category or application. This study aims to assess the suitability of various turbulence models for the Fontan CPAD and to correlate the RANS CFD predictions with experimental results and an LES benchmark.

In traditional turbomachines, the emphasis is to achieve high efficiency. This leads to designs with tight tip clearance for open impeller configurations and small leakage path clearance between the impeller and the shroud for closed impeller configurations. The SST model is well documented to provide good agreement with experiments [15–17] for conventional turbomachinery. However, the Fontan CPAD is intentionally designed to be highly non-obstructive to eliminate the risk of venous pathway obstruction. The gap between the impeller and the housing is large. Thus, if the pump fails, it would still act as an efficient static flow diverter. This non-traditional design further necessitates a comparison of suitable turbulence models to accurately predict the performance of the Fontan CPAD as discussed below. The novel contributions of the present work include:

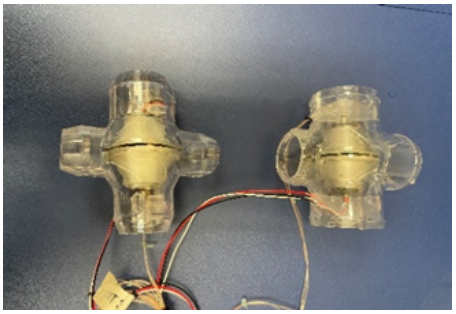

Fig. 1 CPADs with blade heights of 1.09 and 1.62 mm for testing in a mock circulatory loop

- Non-obstructive CPAD design for Fontan procedure and patient safety
- Experimental measurement of head rises across a Fontan CPAD
- Detailed CFD flow study for a Fontan CPAD, including a bladed, biconical impeller, and biconical motor
- Analyzed RANS CFD turbulence models for Fontan CPAD pressure and shear stress prediction, based on benchmarking against experimental data and LES model results
- Identified large, fictitious stagnation regions as the source of the poor performance of the SST turbulence model for accurately predicting Fontan CPAD head rise
- Recommendations for using RANS CFD models for accurate head rise and shear stress predictions for a Fontan CPAD

2 Methods

2.1 CPAD Test Description. A Fontan viscous impeller pump powered by an outrunner configuration biconical brushless DC motor was fabricated and tested using impeller blade heights of 1.09 mm and 1.62 mm as shown in Fig. 1. The pump is integrated into a TCPC housing, creating a pump package for implantation in place of the TCPC.

The test loop is shown in Fig. 2. Major components in the loop emulate the upper and lower body, left and right lungs, superior vena cava (SVC), inferior vena cava (IVC), left pulmonary artery (LPA), and right pulmonary artery (RPA). The in vitro study demonstrated a desirable 11 mmHg head rise at 2400 RPM at 5 LPM (liters/min) with a blade height of 1.62 mm. A 1.09 mm blade height yielded a similar head rise at 3000 RPM. Both achieved a desirable flat HQ curve conducive to consistent performance across a wide range of metabolic activity. The pressure gradient at 0 RPM was less than 0.5 mmHg as compared to a blank TCPC housing with no pump, which is a critical fail-safe result. The measured HQ curves are shown in Fig. 3. These results confirm that a single impeller Fontan pump can provide adequate performance with minimal potential for venous pathway obstruction in the event of device dysfunction. A Fontan pump intended for long-term biventricular maintenance and implanted in series in the Fontan circuit must have no potential for venous pathway obstruction.

Journal of Biomechanical Engineering. Received December 06, 2022;
Accepted manuscript posted August 03, 2023. doi:10.1115/1.4063088

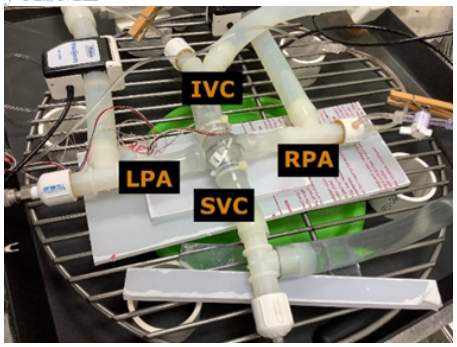

Fig. 2 Mock circulatory test loop for measuring head-flow (HQ) characteristics of a Fontan CPAD

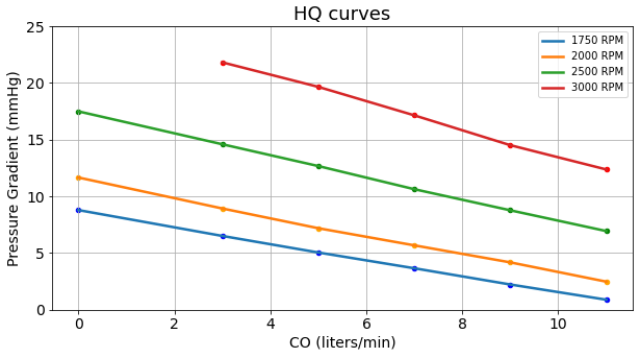

Fig. 3 Measured CPAD pump head vs. flowrate at 4 separate speeds (RPM)

2.2 CFD Theory and Model Description.

2.2.1 Theory. Any incompressible flow, including blood, is characterized by the continuity and Navier-Stokes shown in Eq. (1) and (2). These nonlinear partial differential equations are based on the principles of conservation of mass and momentum. CFD utilizes a numerical solution to these governing equations. The continuous spatial domain of interest is discretized into a finite number of small volumes, known as a mesh. These equations are then solved at the discrete nodes of the mesh using numerical methods such as finite volume and finite difference methods.

$$\frac{\partial \rho}{\partial t} + \frac{\partial (\rho u)}{\partial x} + \frac{\partial (\rho v)}{\partial y} + \frac{\partial (\rho w)}{\partial z} = 0 \tag{1}$$

$$\rho \frac{Du}{Dt} = -\nabla p + \nabla \cdot \tau + \rho g \tag{2}$$

Turbulent flows are ubiquitous in most engineering-related flow domains. Such flows are characterized by rotating flow structures, so-called turbulent eddies, with a wide range of length scales [29]. The largest eddies interact with and extract energy from the mean flow. In this energy cascade mechanism, kinetic energy is transferred from large eddies to progressively smaller eddies as a result of shear in the mean flow [29, 30].

Turbulence models are known to produce more accurate predictions for circulatory assist devices than laminar flow models [31]. RANS modeling is the most widespread approach in industrial applications because of its robustness and computational efficiency. The simulations are focused on the mean flow and the effect of turbulence on mean flow properties. The time averaging operation on the momentum equations in the RANS models discards the details regarding the state of the turbulent eddies in the instantaneous fluctuations and produces mathematically stress-like extra terms called the Reynolds stress. All RANS models aim to represent the effect of turbulence via the closure of these unknown Reynolds stress terms. The most popular RANS models, such as $k-\epsilon$, $k-\omega$, and SST models, are based on Boussinesq assumptions. Boussinesq proposed in 1877 that Reynolds stresses might be proportional to mean strain rates as shown in Eq. (3), where τ_{ij} is the Reynolds stress, U is mean flow velocity, u is fluctuation velocity, μ_t is the turbulent eddy viscosity and k is the turbulent kinetic energy per unit mass. μ_t is proportional to the product of a turbulent velocity scale (V_t), and a turbulent length scale (l_t) as shown in Eq. (4).

$$\tau_{ij} = \mu_t \left(\frac{\partial U_i}{\partial x_j} + \frac{\partial U_j}{\partial x_i} \right) - \frac{2}{3} \rho k \delta_{ij} \tag{3}$$

$$\mu_t = \rho c_\mu V_t l_t \tag{4}$$

The main difference between different RANS models is their approach to modeling the turbulent velocity and length scale. In the $k-\epsilon$ model $\mu_t \sim k^2/\epsilon$, while in the $k-\omega$ model $\mu_t \sim k/\omega$. All RANS models have some limitations due to the modeling assumptions used to derive the mathematical formulation of the model. In general terms, this approach is considered to give satisfactory results when dealing with flows where turbulent fluctuation scales are small. More sophisticated scale-resolving modeling approaches such as LES and DNS are required to resolve complex flow fields [32].

This work compares a wide range of turbulence models from the RANS, LES, and hybrid model families. Predictions from these models are compared with experimental measurements. The $k-\epsilon$ model is the most popular and the most validated RANS model. It emphasizes the mechanisms that determine the kinetic energy of turbulent flows [29]. It solves two additional transport equations for turbulence kinetic energy (k) and turbulence eddy dissipation (ϵ), to model the flow. It is useful for flows without large adverse pressure gradients. It gives good results for wall-bounded and internal flows where mean pressure gradients are small.

The SST $k-\omega$ is another two-equation eddy viscosity turbulence model that combines the $k-\omega$ model formulation in the inner parts of the boundary layer and switches to $k-\epsilon$ behavior in free stream. It uses a blending function to achieve a seamless transition between the two models. It is used in cases with large adverse pressure gradients and separating flows. However, according to studies by Tan et al. [33] and Oliver et al. [34], it over-predicts turbulence in regions of stagnation and strong acceleration.

In a turbulent flow, most of the energy is contained in the larger eddies. They are more anisotropic, and their behavior is dictated by the geometry of the domain, boundary conditions, and body forces. The small eddies are universal in nature and do not depend on the domain shape and boundary conditions. The LES method involves space filtering of the unsteady Navier-Stokes equations prior to the computations, which passes the large eddies and attenuates eddies smaller than a set cutoff width (usually the mesh size level). The filtered Navier-Stokes equation can be written as:

$$\frac{\partial (\rho U_i)}{\partial t} + \frac{\partial (\rho U_i U_j)}{\partial x_j} = -\frac{\partial p}{\partial x_i} + \frac{\partial}{\partial x_j} \left[\mu \left(\frac{\partial U_i}{\partial x_j} + \frac{\partial U_j}{\partial x_i} \right) \right] + \frac{\partial \tau_{ij}}{\partial x_j} \tag{5}$$

The LES approach directly simulates large eddies by numerically solving the filtered unsteady Navier-Stokes equations and the effect of the rejected small eddies is added to the solution employing a so-called sub-grid scale (SGS) model. The Wall-adapting Local Eddy-viscosity (WALE) SGS model was utilized in this study. It is an algebraic model that overcomes some known shortcomings of the standard SGS models such as the Smagorinsky 1963 model [35]. The WALE model [32, 36] produces almost no eddy-viscosity in wall-bounded flows and is therefore capable of reproducing laminar to turbulent transition [37]. LES modeling offers an increased range of applicability, and the resolution of

turbulent structures is more accurate in comparison to RANS simulations [31, 38]. LES models are expensive due to their transient nature, timestep, and grid spacing requirements. The mesh should be sufficiently fine to capture most of the energy-containing eddies. Although LES is more expensive than RANS simulations, its computational time and cost are significantly lower than that of DNS, making it a promising approach for turbulent flow simulations.

The hybrid RANS-LES model takes advantage of the LES model while retaining the computational efficiency of RANS models. The eddies are very small in the boundary layer near the wall and the mesh requirement near the wall is very expensive. Due to the high computational cost of the LES model in the near-wall region, hybrid models are favorable for wall-bounded flows with high Reynolds numbers. The Detached Eddy Simulations (DES) and Stress Blended Eddy Simulations (SBES) [39] are among the most widely used hybrid RANS-LES models. These models utilize LES modeling away from the wall and RANS modeling near the wall [31]. The SBES hybrid model has been utilized in this work. It uses a shielding function f_s to explicitly switch between different RANS and LES turbulence models. In the SBES model, the turbulence stress tensor is defined as:

$$\tau_{ij}^{SBES} = f_s \tau_{ij}^{RANS} + (1 - f_s)\tau_{ij}^{LES} \tag{6}$$

The SBES model provides a rapid transition from the RANS to the LES region, and RANS and LES regions can be easily visualized by plotting the shielding function f_s.

2.2.2 Fontan CPAD CFD model. The Fontan CPAD was designed as a biconical impeller that draws inflow from the superior and inferior vena cava and directs the outflow toward the left and right pulmonary arteries. The pump utilizes an outrunner motor configuration, with a hub-centric biconical stator and rotating impeller blades surrounding the stator. Figure 4 shows the cross-sectional view of the device's computational domain. An internal flow path between the rotor and stator functions as an inherent centrifugal pump and serves to dissipate heat and lubricate the bearing. The housing is a double-inlet double-outlet case in which the pump is structurally suspended, with the IVC and SVC as inlets, and the LPA and RPA as outlets. This design eliminates external motor components which may impair anatomic fit and could represent thermal risk due to fixed-tissue contact.

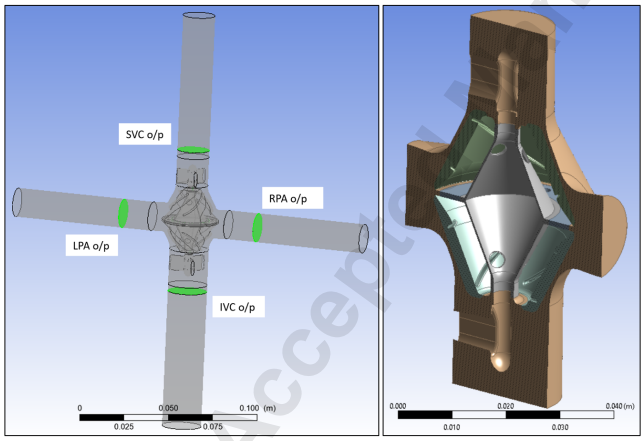

Fig. 4 CAD model of the Fontan CPAD

For CFD modeling, additional tubes were added at the end of the CPAD inlets and outlets to ensure that the pressure boundary conditions imposed at the outlets are sufficiently downstream of the pump exit. The measurements for the static pressure for the inlets and outlets were taken 4 cm from the centerline of the pump, as shown in Fig. 4. The boundary conditions for the CFD study were static pressure at the outlets and mass flow rate at the inlets. The respective pressures and flow rate boundary conditions varied with the total flow rate (cardiac output) and the rotation speed of the pump. The inlet flow was split 40%-60% between the SVC-IVC, respectively. The rotation speeds considered for this study are 2000, 2500, and 3000 RPM, while the total cardiac outputs considered are 3, 5, 7, and 9 LPM. A no-slip boundary condition was assigned to the stationary walls. The outlets were assigned an opening boundary condition to allow for backflow if it is numerically determined. Four RANS turbulence models, $k-\epsilon$, RNG $k-\epsilon$, Realizable $k-\epsilon$, and SST, were considered in this study.

The CFD pre-processing, solving, and post-processing were done on the ANSYS software package (ANSYS Inc., Canonsburg, PA). The meshing was performed using ANSYS Meshing and ICEM CFD software. Inflation layers were used in all the meshes utilized in this study. ANSYS CFX was used for the simulations in the study. Since the realizable $k-\epsilon$ turbulence model was not available in Ansys CFX, this model was simulated using Ansys Fluent CFD package. To simulate the properties of blood, an incompressible Newtonian model with a density of 1098 kg/m^3 and dynamic viscosity of 3.237 cP was used. These values were chosen to match the properties of the fluid used in the experiments. To capture the rotating motion of the CPAD impeller, the entire domain was split into a rotating domain containing the impeller blades and a stationary domain containing the rest of the fluid. Transient rotor-stator interface was used in CFX to simulate the rotating motion of the rotor. A second-order backward Euler transient scheme was used to solve the transport equations. Simulations were considered converged when the residuals were below 10^{-4} and repetitive periodic patterns were observed for the monitored variables.

2.2.3 Grid Independence Study. A grid independence study was performed to ensure that the CFD results were independent of further mesh refinement. The three mesh sizes simulated for this study are shown in Fig. 5 (a), (b), (c): Mesh 1 (5.54 million elements), Mesh 2 (11.41 million elements), and Mesh 3 (16.51 million elements). Table 1 provides the results for the pressure head for the three meshes considered using the $k-\epsilon$, RNG $k-\epsilon$, and SST models.

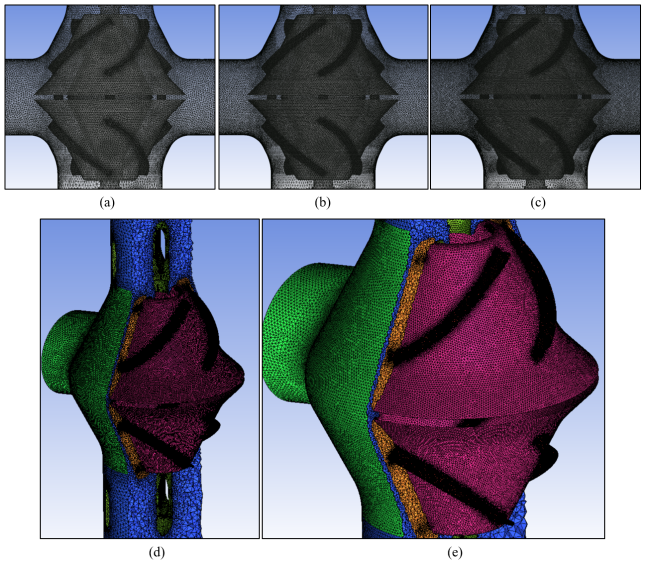

Fig. 5 Computational domain: The meshes chosen for the grid independence study: (a) Mesh 1, (b) Mesh 2, (c) Mesh 3, (d) and (e) 3D view of Mesh 2 with the impeller blades and housing cross-section

The difference in pressure head between Mesh 2 and Mesh 3 is 0.4% on average, whereas the difference between Mesh 1 and Mesh

Table 1 Results of the grid independence study

Turbulence model	Pressure head [mmHg]		
	Mesh 1	Mesh 2	Mesh 3
SST	9.91	9.26	9.21
$k-\epsilon$	17.62	17.15	17.07
RNG $k-\epsilon$	13.62	12.74	12.76

	Pressure head [mmHg]	Torque [Nm]
LES - Mesh 1	15.73	$6.75E{-}03$
LES - Mesh 2	16.25	$6.77E{-}03$
LES - Mesh 3	15.91	$6.81E{-}03$

2 is 6%. Since the results with Mesh 2 and Mesh 3 were nearly identical, Mesh 2 was used for all further RANS CFD simulations as it reduced the computation time compared to Mesh 3. The y+ value for the chosen mesh was less than 2 on the rotating domain and the housing, and less than 3.5 on the additional tubes attached to the end of the CPAD.

The mesh requirements for LES are much more stringent than those for RANS. Therefore, to check for grid independence of LES results three additional finer meshes were generated for simulating the Fontan CPAD using LES. They consisted of approx. 27 million, 39 million, and 62 million elements respectively. The pressure head and torque values for these meshes are compared in Table 1. The maximum deviation for the pressure head is 3.1%, while the results for the total torque deviate by 0.8%. Thus, the results for the LES model are observed to be grid independent. For the analysis of LES results, the LES Mesh 2 was chosen.

3 Results

3.1 RANS models. The pressure head for the CPAD was calculated as the difference between the average static pressure at the two outlets and two inlets. A typical plot for the pressure head vs. time is shown in Fig. 6. The plot shows the fluctuating component of the pressure head as well as a running average taken over 10 revolutions. The values reported as pressure heads in this paper are the running averages taken for each simulation. The fluctuations are consistent with the 4-bladed impeller design of the pump. For each revolution of the pump, 4 peaks/valleys are observed in the waveform.

The pressure head was calculated for the rotation speeds of 2000-3000 RPM and a total flow rate of 3-9 LPM. These cases were run for $k-\epsilon$, RNG $k-\epsilon$, Realizable $k-\epsilon$, and SST turbulence models, and pressure performance HQ curves were generated as shown in Fig. 7. The static pressure head across the pump for a given speed decreases with increasing flow rate. This trend is seen for all the turbulence models as well as the experimental results. As observed from Fig. 7, the SST turbulence model shows the largest deviation of pressure head from the experimental results across all cases. It is seen to be under-predicting the pressure head. Table 2 shows the pressure head values for all turbulence models across flow rates and speeds. As the total flow rate increases, the $k-\epsilon$ turbulence model shows better agreement with the experimental results. However, for RNG $k-\epsilon$, Realizable $k-\epsilon$, and SST turbulence models, the deviation from experiments increases with increasing flow rates. This trend is consistent for all speeds considered in this study.

Since the variability in the results between the $k-\epsilon$, RNG $k-\epsilon$, Realizable $k-\epsilon$, and SST turbulence models was very high, two additional RANS turbulence models, Generalized $k-\omega$ (GEKO) and SST with transitional turbulence, were analyzed in this study. To save computation time, only one configuration (3000 RPM, 7 LPM) was simulated for these two additional RANS models. The models were run with the default parameters. For the GEKO model, 2 different values for the separation coefficient parameter (1 and 1.75)

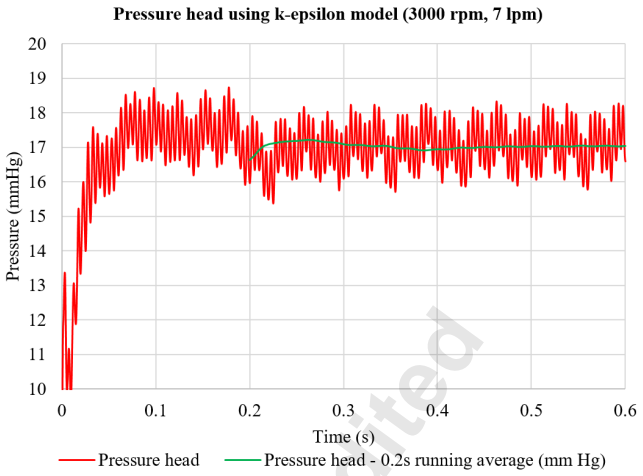

Fig. 6 Pressure head for $k-\epsilon$ turbulence model (3000 RPM, 7 LPM configuration)

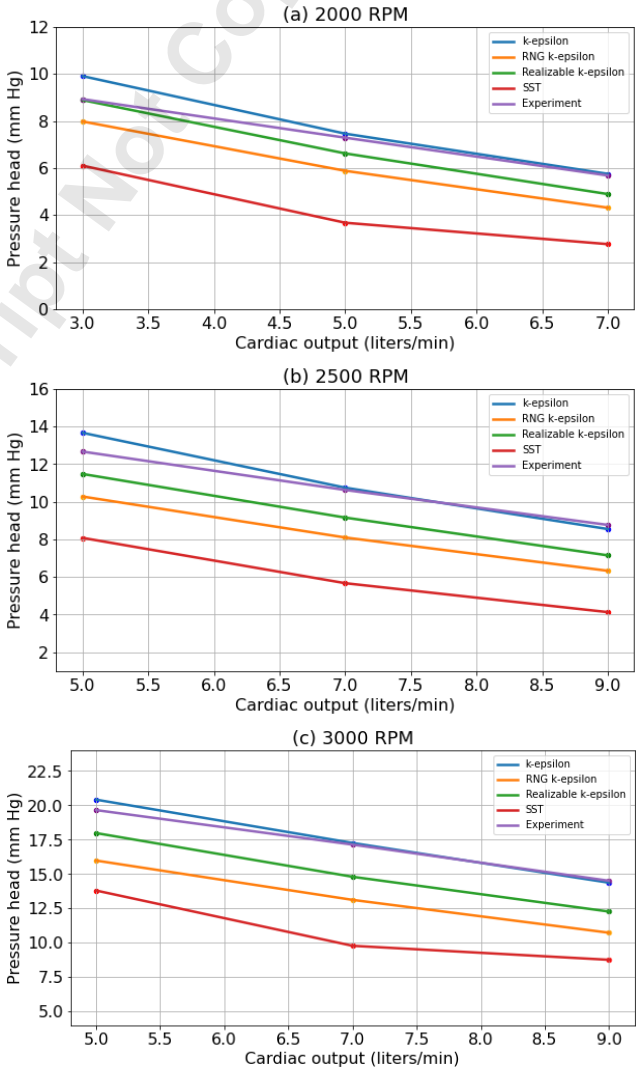

Fig. 7 HQ curves for the Fontan CPAD comparing the three turbulence models with experimental results: (a) 2000 rpm (b) 2500 rpm (c) 3000 rpm

Table 2 Pressure head [mmHg] for experiment and turbulence models

	2000 RPM					
	3 LPM		5 LPM		7 LPM	
	Head	% diff	Head	% diff	Head	% diff
Experiment	8.93		7.29		5.68	
$k-\epsilon$	9.91	10.97	7.46	2.33	5.75	1.23
RNG $k-\epsilon$	7.98	−10.64	5.88	−19.34	4.31	−24.12
Realizable $k-\epsilon$	8.89	−0.45	6.62	−9.19	4.89	−13.91
SST	6.10	−31.69	3.67	−49.66	2.76	−51.41

	2500 RPM					
	5 LPM		7 LPM		9 LPM	
	Head	% diff	Head	% diff	Head	% diff
Experiment	12.67		10.63		8.77	
$k-\epsilon$	13.67	7.89	10.75	1.13	8.55	−2.51
RNG $k-\epsilon$	10.28	−18.86	8.10	−23.80	6.33	−27.82
Realizable $k-\epsilon$	11.48	−9.39	9.16	−13.83	7.15	−18.47
SST	8.08	−36.23	5.67	−46.66	4.13	−52.91

	3000 RPM					
	5 LPM		7 LPM		9 LPM	
	Head	% diff	Head	% diff	Head	% diff
Experiment	19.65		17.14		14.51	
$k-\epsilon$	20.41	3.87	17.26	0.70	14.37	−0.96
RNG $k-\epsilon$	15.98	−18.68	13.12	−23.45	10.73	−26.05
Realizable $k-\epsilon$	17.98	−8.50	14.8	−13.65	12.27	−15.44
SST	13.80	−29.77	9.78	−42.94	8.76	−39.63

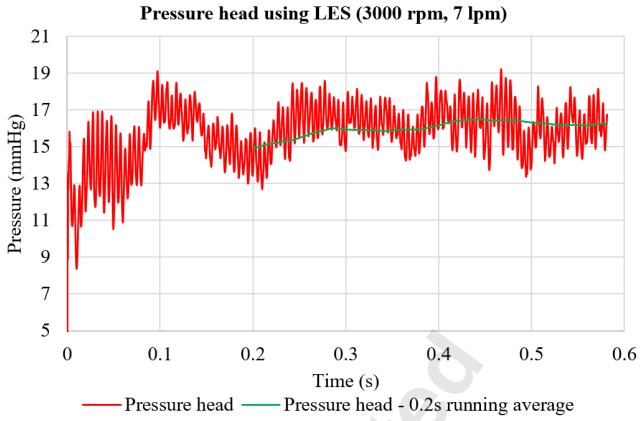

Fig. 8 Pressure head prediction using LES (3000 RPM, 7 LPM configuration)

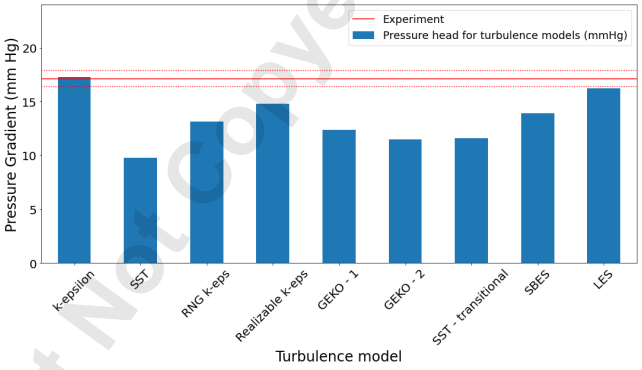

Fig. 9 Pressure head results for all turbulence models (3000 RPM, 7 LPM configuration) along with experimental result and its uncertainty (dotted line)

were chosen. The pressure head predicted using the separation coefficient of 1 for the GEKO model was 12.35 mmHg, and 11.5 mmHg when the separation coefficient was 1.75. With the SST model using transitional turbulence, the predicted pressure head was 11.5 mmHg. The experimentally measured value was 17.14 mmHg. Assuming the instrumentation and catheter position errors are all independent, there was a total of ±0.75 mmHg experimental uncertainty of head, for a cardiac output (CO) of around 7 LPM. The pressure head results for the turbulence models and the experimental value with its uncertainty of ±0.75 mmHg are shown in Fig. 9.

3.2 LES and SBES models. Since the variation between the RANS models was very high, the authors decided to test a non-RANS model to compare with the RANS and experimental results. A high-fidelity LES, specifically the WALE LES model, was chosen to be the arbiter between the models, and the configuration of 3000 RPM pump speed and 7 LPM flow rate was simulated. For the chosen case, the LES model predicted a pressure head of 16.25 mmHg. This prediction is much closer to the $k-\epsilon$ turbulence model and the experimental results (-5.2% deviation with experiment, -5.9% with $k-\epsilon$, and 61% with SST). The predicted pressure head waveform and the moving average over 10 revolutions are shown in Fig. 8.

Additionally, a hybrid RANS-LES model SBES was also simulated. The same mesh that was used for the RANS models was used for the SBES model. The pressure head predicted was 13.94 mmHg. An additional simulation was also performed with the SBES turbulence model using the LES mesh. The pressure head predicted with this mesh was approximately 16 mmHg. This shows that, unlike the RANS models, the SBES turbulence model cannot be simulated using RANS Mesh 2, it requires further refinement of the mesh.

3.3 Laminar model. To analyze the importance of turbulent effects in the CPAD, a laminar model was simulated for the 3000 RPM, 7 LPM configuration. The pressure head predicted by the laminar model was 10.24 mmHg. This shows a deviation of 40.3% from the experimental head prediction. Most of the turbulence models analyzed in this study predicted more accurate results for the head than the laminar model. It has been shown in [32] that turbulence models make better predictions than laminar model for circulatory assist devices. The pressure head predictions from the CPAD further reinforce this statement.

For a pump, the global Reynolds number is approximated as $Re = \rho\omega D^2/\mu$ using impeller diameter (D) as the characteristic length [23]. The constants ρ, ω, μ are the fluid density, angular speed, and dynamic viscosity, respectively. Using this definition for the CPAD, the Reynolds number is of the order 10^4. Thus, turbulent flow conditions were expected to dominate. This is reflected in the high deviation of the pressure head for the laminar model from the experiments, as compared to other turbulence models.

4 Discussion

4.1 Comparison between SST, $k-\epsilon$, and LES models. Figure 10 shows the static pressure distribution across the CPAD along a cross-section passing through the center of the pump and slicing through the outlets. The pressures were normalized with respect to the static pressure at SVC inlet as a reference to ensure that all turbulence models show a pressure change with respect to the same

Journal of Biomechanical Engineering. Received December 06, 2022;
Accepted manuscript posted August 03, 2023. doi:10.1115/1.4063088

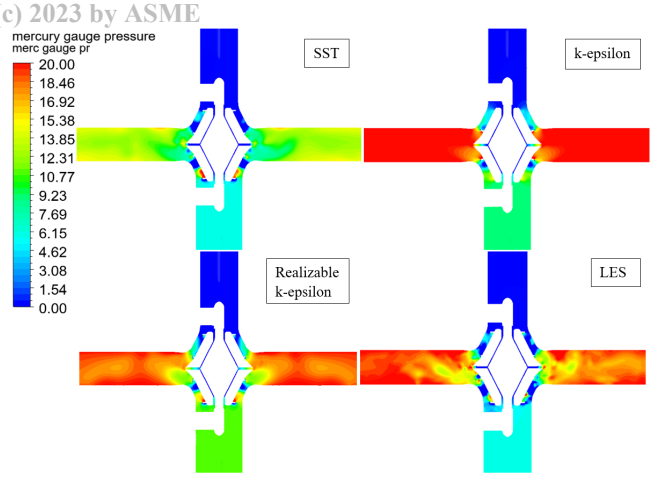

Fig. 10 Comparison of pressure (in mmHg) for SST, $k-\epsilon$, Realizable $k-\epsilon$, and LES turbulence models

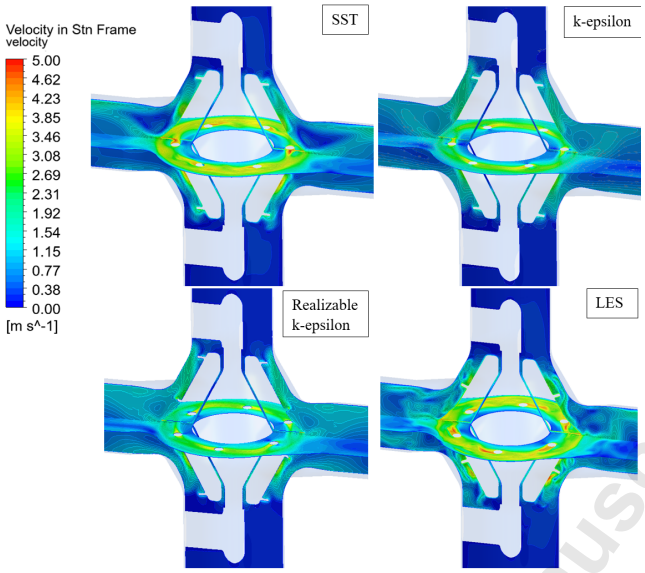

Fig. 11 Velocity contour plots in two cross-sections along the centerline of the CPAD for SST, $k-\epsilon$, Realizable $k-\epsilon$, and LES models

value. Thus, in the below plots, the SVC pressure is 0 mmHg, and we can visualize the pressure head going from the inlets to the outlets. Across all models, the pressure can be seen gradually increasing across the pump from the inlets to the outlets. Additionally, the pressure at the outlets for SST is much lower than for LES and $k-\epsilon$, which is consistent with the pressure head values seen in Table 2.

The velocity contour plots for the SST, $k-\epsilon$, and LES models across two different cross-sections passing through the center of the CPAD are shown in Fig. 11. The wakes present behind the equatorial posts in the LES model are also seen in the SST model with similar velocity values. In the $k-\epsilon$ model, these wakes are present with less intensity, as evident due to the lack of red regions.

In traditional turbomachinery, SST has been the preferred turbulence model for CFD analysis [15–17]. However, in the Fontan CPAD, the pressure head predicted by the SST model deviated by as much as 53% from the experiments. An analysis was conducted to investigate the potential explanation for this large discrepancy. To explain the disparity in the static pressure values across the turbulence models, the velocity contour plots for SST, LES, and $k-\epsilon$ turbulence models for various phases in one rotation cycle of

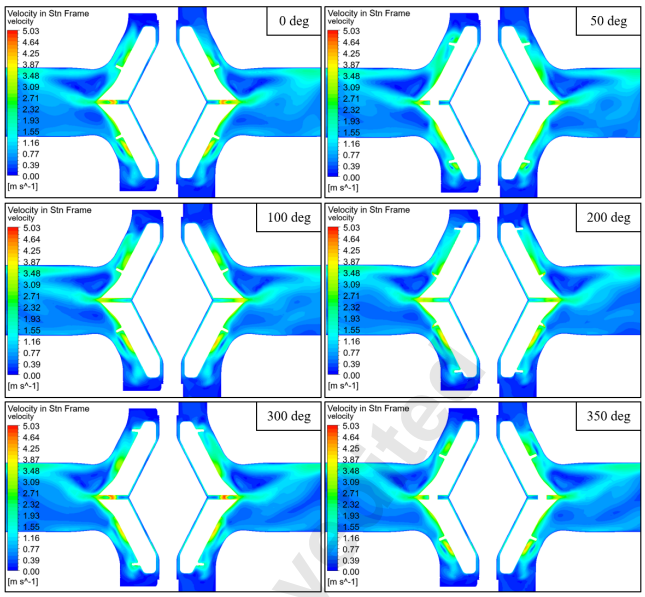

Fig. 12 SST velocity contour plots

the CPAD were plotted in Fig. 12, 13, and 14. The same cross-section was chosen as the one for demonstrating the static pressure in Fig. 10. An arbitrary phase was chosen as the starting point (0°). Subsequent plots were generated for various phases in one rotation of the pump.

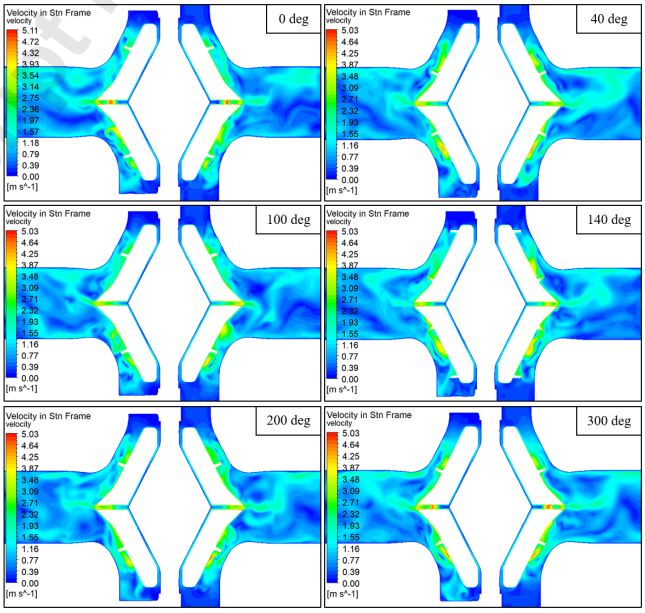

Fig. 13 LES velocity contour plots

The most significant difference observed between the three models is the presence of recirculation zones near the pump outlets in the SST model. These recirculation zones persist in all the phases in one cycle of the pump. These zones are much weaker in the LES and the $k-\epsilon$ models. To better visualize these recirculation zones, one phase was chosen for the three models and the velocity scale was adjusted from 0-0.8 m/s. Figure 15 shows this prominent stagnation region in SST as compared to LES and $k-\epsilon$. The presence of the persistent recirculation zones in the SST turbulence model is an indication of the lower efficiency of the turbulence model and consequently, an under-prediction of the head rise.

Journal of Biomechanical Engineering. Received December 06, 2022;
Accepted manuscript posted August 03, 2023. doi:10.1115/1.4063088

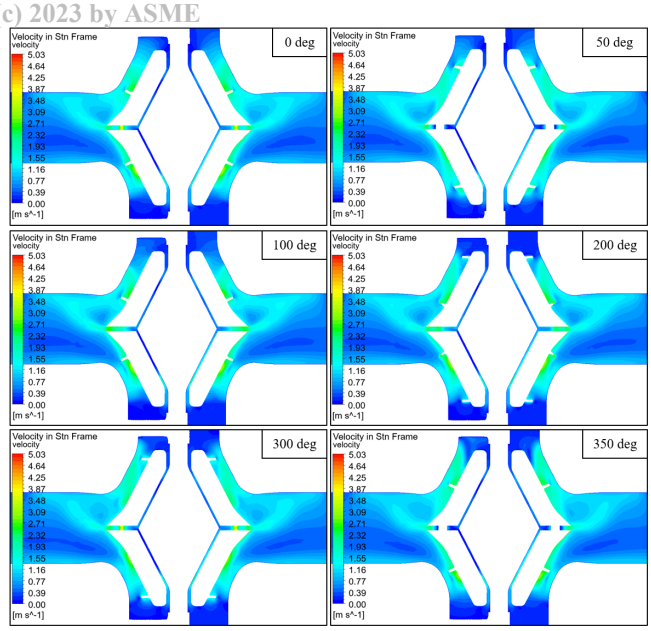

Fig. 14 $k-\epsilon$ velocity contour plots

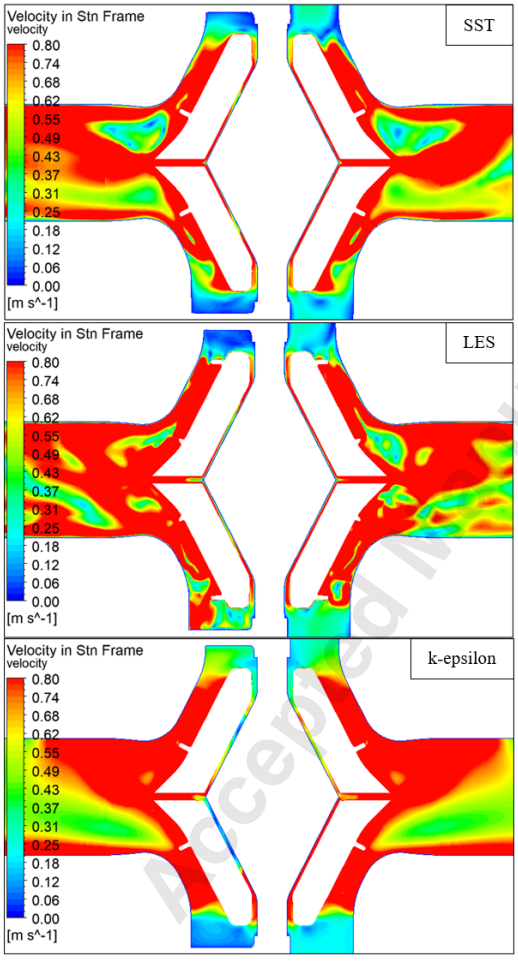

Fig. 15 Velocity contour plots comparing the low velocity zones

4.2 Comparison of torque and shear stress. Figure 16 shows a comparison between the wall shear stress at the impeller surface. The wall shear stress from the SST turbulence model

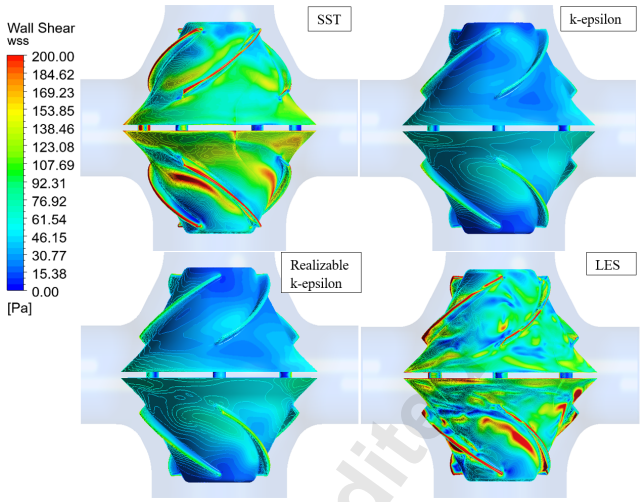

Fig. 16 Wall shear stress on the rotor for SST, $k-\epsilon$, Realizable $k-\epsilon$, and LES turbulence models

matches better with the LES model across the entire rotor surface, particularly near the impeller blades. The $k-\epsilon$ model appears to under-predict the wall shear stress throughout the surface. This behavior can also be seen in Table 3 where the torque on the rotor is compared. The total torque values are similar for the SST and LES models (4.8% difference), whereas the $k-\epsilon$ and RNG $k-\epsilon$ models under-predict the torque values (29% difference).

Additional parameters such as the torque on the secondary flow path (described as the internal path between rotor and stator in section 2.2.2), as well as the flow rate from the secondary path, are compared in Table 3. The secondary path flow rate for the SST, RNG $k-\epsilon$, and LES are almost identical (less than 4% variation) whereas the $k-\epsilon$ turbulence model under-predicts this value by 15%.

Table 3 Comparing torque and secondary path flow rate across turbulence models

	Total rotor torque [Nm]	Secondary path torque [Nm]	Secondary path flow rate (liters/min)
SST	$7.10E{-}03$	$1.07E{-}03$	0.8
$k-\epsilon$	$4.79E{-}03$	$5.74E{-}04$	0.68
RNG $k-\epsilon$	$4.74E{-}03$	$6.06E{-}04$	0.77
Realizable $k-\epsilon$	$4.89E{-}03$	$6.22E{-}04$	0.79
LES	$6.76E{-}03$	$9.90E{-}04$	0.81

4.3 Sensitivity of turbulence models to geometry changes in the CPAD. The results discussed in the previous sections focused on one geometry of the CPAD. To investigate the sensitivity of the turbulence models to any geometry changes, a design variation of the CPAD model was analyzed. Since the impeller blades are mainly responsible for the pressure head generation in the CPAD, a new model with blade height equal to 75% of the blade height of the original model was generated and meshed. To analyze if the results for this model followed the same trends as the original design, this model was simulated using SST, $k-\epsilon$, and LES models. The pressure head predicted by the $k-\epsilon$ model was 10.9 mmHg, whereas, for the LES and SST models, the predicted head was 9.44 mmHg and 4.85 mmHg, respectively. Firstly, this shows that the blade height change represents a notable change in the geometry since the head predicted by each of the models is significantly different from their respective predictions for the original design.

Additionally, LES predicts a 13% lower head as compared to the $k-\epsilon$, and a 49% higher head as compared to the SST model. These trends are similar to those observed in the original design.

4.4 Comparison of run-time required for each turbulence model. RANS models are preferred for engineering applications due to their low computation times. High-fidelity models such as LES have a major disadvantage in that they are computationally expensive. Table 4 provides the computation resources (CPU hours – calculated as the number of processing cores multiplied by the wall clock time) required for each model.

Table 4 Comparison of time required for each model (ref. $k-\epsilon$: 18 hours wall clock time using 64 cores)

Turbulence model	Pressure head [mmHg]	Total rotor torque [Nm]	CPU hours (# cores * wall clock time)	Time compared to $k-\epsilon$
$k-\epsilon$	17.26	$4.79E{-}03$	1799.24	1.0
SST	9.78	$7.10E{-}03$	2016.00	1.12
RNG $k-\epsilon$	13.12	$4.74E{-}03$	1817.86	1.01
Realizable $k-\epsilon$	14.8	$4.89E{-}03$	1770.67	0.99
GEKO - 1	12.35	$7.12E{-}03$	2094.86	1.16
GEKO - 2	11.5	$7.13E{-}03$	1995.14	1.11
SST transitional	11.62	$7.16E{-}03$	2761.90	1.54
SBES	13.94	$6.74E{-}03$	4067.80	2.26
LES Mesh 2	16.25	$6.77E{-}03$	12061.86	6.70
LES Mesh 3	15.91	$6.81E{-}03$	19275.23	10.72

4.5 Tuning the SST turbulence model with the A1 parameter. Since the SST turbulence model under-predicted the pressure head in the CPAD, a logical step was to tune the model and assess the impact of varying the parameters for the SST model. When the model over-predicts the separation region, the recirculation zone is extended. This can be controlled by varying the A1 parameter in the SST model settings. The default value of A1 is 0.31 and to address the extended recirculation region, ANSYS documentation [38, 40] recommends increasing the value of A1, with the maximum value being 1.

A parametric study involving various values of A1 was performed. Increasing the A1 parameter from the default value of 0.31 to 0.6 increases the predicted head rise to 10.7 mmHg. Further increasing A1 to 0.9, the head rise increases to 11.4 mmHg. Thus, increasing A1 helps in increasing the head rise closer to the experimental values. However, the recirculation zones observed near the outlets do not appear to be eliminated as seen in Fig. 17, and the pressure head is still much lower than the experiment.

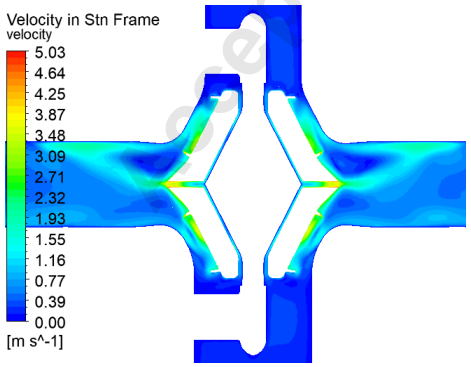

Fig. 17 Velocity contour plots for SST with $A1 = 0.9$

5 Conclusion

Traditional turbomachines are designed to be as efficient as possible. This leads to very small tip clearances between the blades and the housing to minimize leakage. However, the Fontan CPAD is, by design, intended to have low efficiency due to its unique application and low head requirement. It is an imperative safety constraint to avoid obstruction risk in the passive flow case, i.e., pump dysfunction. The CPAD is intended to act as a flow diverter in stalled condition. Small tip clearances in such a scenario would increase the chances of blood stasis near the blades and consequently increase the risk of thrombosis. Increasing the tip clearances mitigate this issue at the cost of efficiency. Additionally, the greater tip clearance reduces the internal resistance (measured in mmHg/LPM) of the pump. This enables the pump to produce a nearly flat HQ curve. A patient's metabolic needs change with level of activity causing a need to increase cardiac output. The flat HQ curve allows for nearly constant head rise across a typical cardiac output ranging from 4 to 11 LPM. Due to such an unconventional turbomachinery design, the choice of CFD turbulence models was analyzed in the study. The results strongly indicate a need to verify the conventional use of SST for rotating machinery CFD flow modeling when large clearances exist in a design. They also suggest validating the results using an LES, other non-RANS models, or test results if economically feasible.

A correlation study with results from the experiments was performed. The study showed inferior performance of the SST model in predicting the pressure head across the CPAD. Even with tuning the parameters such as A1, the head rise results did not correlate well with the experiments. The results from the SST model were confirmed by obtaining nearly identical predictions using SST modeling studies at 2 different organizations using different software (CFX and STAR-CCM) and different meshes. This result is contrary to typical rotating machinery flow modeling which relies heavily on SST for providing accurate predictions.

In contrast, the $k-\epsilon$ model showed excellent agreement with the measured head rise across all analyzed conditions of flow rates and speeds. A high-fidelity LES model was also employed as an arbiter to compare the results between the other RANS models. The LES and $k-\epsilon$ models predicted similar pressure heads (LES predicted a 5.8% lower head rise than $k-\epsilon$). In contrast, for the torque and the wall shear stress, the SST model predicted values similar to LES (SST predicted 4.8% higher torque than LES). Thus, the LES model validates the correctness of the $k-\epsilon$ model in predicting the head rise and of the SST model in predicting the torque and shear stress. The flow was also modeled for a notable change to the blade height, a dominant feature for affecting head rise. While the LES and $k-\epsilon$ head rise predictions were again highly similar, the SST prediction was 49% lower than LES. This supports the continued use of the $k-\epsilon$ model for optimization of the CPAD for head rise.

LES is always the preferred approach over RANS models for its superiority in predicting head rise and shear stresses, however, its use is not always economically feasible. In the latter case, for the Fontan CPAD, with large blade tip clearance and small blades, it is recommended to use $k-\epsilon$ for head and general flow simulation and SST for power and shear stress predictions. This conclusion cannot be extended to the general case of VADs or other centrifugal pumps, but it does raise a cautionary note to benchmark RANS model results with LES or test data whenever possible.

The relative importance of accurate prediction of the head rise and shear stress for the Fontan CPAD is still under investigation. In that regard, hemolysis tests conducted by the coauthor at the University of Louisville show the effect of shear stress on hemolysis may be minor since the modified index of hemolysis (MIH) value of 2.296 for a prototype Fontan CPAD is well below comparable values measured on VADs, as shown in Fig. 18 [41]. The effect of shear stress on thrombosis in the Fontan CPAD will be tested at the University of Oregon in the near future.

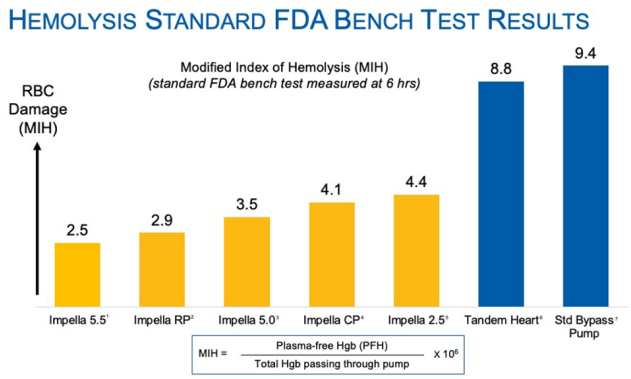

Fig. 18 Hemolysis standard FDA bench test results

Acknowledgment

We gratefully acknowledge funding provided by the National Institutes of Health (NIH). Portions of this research were conducted with the advanced computing resources provided by Texas A&M High Performance Research Computing. Finally, we thank Mike Neary, Victor Obeid, and Ed Marlinski of RBTS Inc. for developing the CPAD hardware utilized in the tests at Clemson University and providing solid models for the CFD studies.

Funding Data

This work was funded by an NIH grant under award number R01HL150346

References

[1] Fontan, F. and Baudet, E., 1971, "Surgical repair of tricuspid atresia," Thorax, **26**(3), pp. 240–248.
[2] Rodefeld, M. D., Boyd, J. H., Myers, C. D., LaLone, B. J., Bezruczko, A. J., Potter, A. W., and Brown, J. W., 2003, "Cavopulmonary assist: circulatory support for the univentricular Fontan circulation," The Annals of thoracic surgery, **76**(6), pp. 1911–1916.
[3] Ali, M. S., Mortazavi, F., and Palazzolo, A., 2020, "Flow Field Instability and Rotordynamic Impedances for an Open Impeller Centrifugal Pump in Transient Four-Quadrant Regimes," *Turbo Expo: Power for Land, Sea, and Air*, Vol. 84225, American Society of Mechanical Engineers, p. V10BT29A009.
[4] Ali, M. S., Mortazavi, F., and Palazzolo, A., 2021, "System Level Analysis of Compressor Eye-Labyrinth Seal Rotordynamic Forces: A Computational Fluid Dynamics Approach," *Turbo Expo: Power for Land, Sea, and Air*, Vol. 85031, American Society of Mechanical Engineers, p. V09BT28A004.
[5] Ali, M., Pandey, N., Hadj-Nacer, M., Greiner, M., and Riyad, M. F., 2021, "Parametric study of two-phase flow in a porous wick of a mechanically pumped loop heat pipe," *AIP Conference Proceedings*, Vol. 2324, AIP Publishing, Paper No. 1.
[6] Zhang, J., Zhang, P., Fraser, K. H., Griffith, B. P., and Wu, Z. J., 2013, "Comparison and experimental validation of fluid dynamic numerical models for a clinical ventricular assist device," Artificial organs, **37**(4), pp. 380–389.
[7] Chua, L. P., Song, G., Lim, T. M., and Zhou, T., 2006, "Numerical analysis of the inner flow field of a biocentrifugal blood pump," Artificial organs, **30**(6), pp. 467–477.
[8] Anderson, J. B., Wood, H. G., Allaire, P. E., McDaniel, J. C., Olsen, D. B., and Bearnson, G., 2000, "Numerical studies of blood shear and washing in a continuous flow ventricular assist device," ASAIO journal, **46**(4), pp. 486–494.
[9] Song, X., Throckmorton, A. L., Wood, H. G., Allaire, P. E., and Olsen, D. B., 2004, "Transient and quasi-steady computational fluid dynamics study of a left ventricular assist device," ASAIO journal, **50**(5), pp. 410–417.
[10] Untaroiu, A., Wood, H. G., Allaire, P. E., Throckmorton, A. L., Day, S., Patel, S. M., Ellman, P., Tribble, C., and Olsen, D. B., 2005, "Computational design and experimental testing of a novel axial flow LVAD," ASAIO journal, **51**(6), pp. 702–710.
[11] Anderson, J. B., Wood, H. G., Allaire, P. E., Bearnson, G., and Khanwilkar, P., 2000, "Computational flow study of the continuous flow ventricular assist device, prototype number 3 blood pump," Artificial Organs, **24**(5), pp. 377–385.
[12] Kido, K., Hoshi, H., Watanabe, N., Kataoka, H., Ohuchi, K., Asama, J., Shinshi, T., Yoshikawa, M., and Takatani, S., 2006, "Computational fluid dynamics analysis of the pediatric tiny centrifugal blood pump (TinyPump)," Artificial organs, **30**(5), pp. 392–399.
[13] Wu, J., Paden, B. E., Borovetz, H. S., and Antaki, J. F., 2010, "Computational fluid dynamics analysis of blade tip clearances on hemodynamic performance and blood damage in a centrifugal ventricular assist device," Artificial organs, **34**(5), pp. 402–411.
[14] Bluestein, D., Rambod, E., and Gharib, M., 2000, "Vortex shedding as a mechanism for free emboli formation in mechanical heart valves," J. Biomech. Eng., **122**(2), pp. 125–134.
[15] Mortazavi, F. and Palazzolo, A., 2017, "CFD-Based Prediction of Rotordynamic Performance of Smooth Stator-Grooved Rotor (SS-GR) Liquid Annular Seals," *Turbo Expo: Power for Land, Sea, and Air*, Vol. 50923, American Society of Mechanical Engineers, p. V07AT34A007.
[16] Mortazavi, F. and Palazzolo, A., 2019, "A Transient Computational Fluid Dynamics, Phase Modulated, Multifrequency Approach for Impeller Rotordynamic Forces," Journal of Fluids Engineering, **141**(7), p. 071110.
[17] Mortazavi, F. and Palazzolo, A., 2018, "Prediction of rotordynamic performance of smooth stator-grooved rotor liquid annular seals utilizing computational fluid dynamics," Journal of Vibration and Acoustics, **140**(3), p. 031002.
[18] Delorme, Y., Anupindi, K., Kerlo, A., Shetty, D., Rodefeld, M., Chen, J., and Frankel, S., 2013, "Large eddy simulation of powered Fontan hemodynamics," Journal of biomechanics, **46**(2), pp. 408–422.
[19] Delorme, Y. T., Rodefeld, M. D., and Frankel, S. H., 2017, "Multiblock high order Large Eddy Simulation of powered Fontan hemodynamics: Towards computational surgery," Computers & fluids, **143**, pp. 16–31.
[20] Burgreen, G. W., Loree, H. M., Bourque, K., Dague, C., Poirier, V. L., Farrar, D., Hampton, E., Wu, Z. J., Gempp, T. M., and Schöb, R., 2004, "Computational fluid dynamics analysis of a maglev centrifugal left ventricular assist device," Artificial organs, **28**(10), pp. 874–880.
[21] Zhang, J., Koert, A., Gellman, B., Gempp, T. M., Dasse, K. A., Gilbert, R. J., Griffith, B. P., and Wu, Z. J., 2007, "Optimization of a miniature maglev ventricular assist device for pediatric circulatory support," Asaio Journal, **53**(1), pp. 23–31.
[22] Song, X., Wood, H. G., Day, S. W., and Olsen, D. B., 2003, "Studies of turbulence models in a computational fluid dynamics model of a blood pump," Artificial organs, **27**(10), pp. 935–937.
[23] Throckmorton, A. L. and Untaroiu, A., 2008, "CFD analysis of a Mag-Lev ventricular assist device for infants and children: Fourth generation design," ASAIO journal, **54**(4), pp. 423–431.
[24] Al-Azawy, M. G., Turan, A., and Revell, A., 2016, "Assessment of turbulence models for pulsatile flow inside a heart pump," Computer methods in biomechanics and biomedical engineering, **19**(3), pp. 271–285.
[25] Al-Azawy, M. G., Turan, A., and Revell, A., 2015, "Investigating the use of turbulence models for flow investigations in a positive displacement ventricular assist device," *6th European Conference of the International Federation for Medical and Biological Engineering: MBEC 2014, 7-11 September 2014, Dubrovnik, Croatia*, Springer, pp. 395–398.
[26] Lui, M., Martino, S., Salerno, M., and Quadrio, M., 2020, "On the turbulence modeling of blood flow in a stenotic vessel," Journal of biomechanical engineering, **142**(1), p. 011009.
[27] Wang, S., Tan, J., and Yu, Z., 2019, "Comparison and experimental validation of turbulence models for an axial flow blood pump," Journal of Mechanics in Medicine and Biology, **19**(08), p. 1940063.
[28] Semenzin, C. S., Simpson, B., Gregory, S. D., and Tansley, G., 2021, "Validated guidelines for simulating centrifugal blood pumps," Cardiovascular Engineering and Technology, **12**, pp. 273–285.
[29] Versteeg, H. K. and Malalasekera, W., 2007, *An introduction to computational fluid dynamics: the finite volume method*, Pearson education.
[30] Pope, S. B., 2000, *Turbulent flows*, Cambridge university press.
[31] Menter, F. R., 2012, "Best practice: scale-resolving simulations in ANSYS CFD," ANSYS Germany GmbH, **1**, pp. 1–70.
[32] Kamali Moghadam, R., Javadi, K., and Kiani, F., 2016, "Assessment of the LES-WALE and zonal-DES turbulence models in simulation of the flow structures around the finite circular cylinder," Journal of Applied Fluid Mechanics, **9**(2), pp. 909–923.
[33] Jie, T. and Jie, J., 2011, "Stress limiter consideration for k-omega turbulence models in shock-wave/turbulent boundary-layer interactions in supersonic and hypersonic flows," *20th AIAA Computational Fluid Dynamics Conference*, p. 3980.
[34] Oliver, A., Lillard, R., Schwing, A., Blaisdell, G., and Lyrintzis, A., 2007, "Assessment of turbulent shock-boundary layer interaction computations using the OVERFLOW code," *45th AIAA Aerospace Sciences Meeting and Exhibit*, p. 104.
[35] Smagorinsky, J., 1963, "General circulation experiments with the primitive equations: I. The basic experiment," Monthly weather review, **91**(3), pp. 99–164.
[36] Weickert, M., Teike, G., Schmidt, O., and Sommerfeld, M., 2010, "Investigation of the LES WALE turbulence model within the lattice Boltzmann framework," Computers & Mathematics with Applications, **59**(7), pp. 2200–2214.
[37] Nicoud, F. and Ducros, F., 1999, "Subgrid-scale stress modelling based on the square of the velocity gradient tensor," Flow, turbulence and Combustion, **62**(3), pp. 183–200.
[38] Ansys, C., 2009, "ANSYS CFX-solver theory guide," Ansys CFX Release, **15317**, pp. 724–746.
[39] Xia, Y., Verma, I., Zore, K., and Sharkey, P., 2020, "SBES/FGM simulation of forced response of a premixed bluff-body stabilized flame," *AIAA Scitech 2020 Forum*, p. 0175.
[40] Ansys, C., 2010, "Solver modeling guide," Release, **11**, pp. 1996–2006.
[41] "Hemolysis FAQ," Abiomed, Inc., accessed June 15, 2021, https://www.heartrecovery.com/education/education-library/faq-hemolysis

Journal of Biomechanical Engineering. Received December 06, 2022;
Accepted manuscript posted August 03, 2023. doi:10.1115/1.4063088

List of Figures

List of Tables